ACS Catalysis

Research Article

pubs.acs.org/acscatalysis

General Method for Determination of the Surface Composition in Bimetallic Nanoparticle Catalysts from the L Edge X-ray Absorption Near-Edge Spectra

Tianpin Wu,[†] David J. Childers,[‡] Carolina Gomez,[‡] Ayman M. Karim,[§] Neil M. Schweitzer,[†] A. Jeremy Kropf,[†] Hui Wang,[⊥] Trudy B. Bolin,[∥] Yongfeng Hu,[¶] Libor Kovarik,[§] Randall J. Meyer,*[,‡] and Jeffrey T. Miller*[,†]

[†]Division of Chemical Sciences and Engineering, [∥]Advanced Photon Source, Argonne National Laboratory, Argonne, Illinois 60439, United States

[‡]Department of Chemical Engineering, University of Illinois at Chicago, Chicago, Illinois 60612, United States

[§]Institute for Integrated Catalysis, Pacific Northwest National Laboratory, Richland, Washington 99352, United States

[⊥]Department of Chemical and Biological Engineering, University of Saskatchewan, Saskatoon, Saskatchewan, Canada S7N 5A2

[¶]Canadian Light Source, Saskatoon, Saskatchewan, Canada S7N 0X4

Supporting Information

ABSTRACT: Bimetallic PtPd on silica nanoparticle catalysts have been synthesized, and their average structure has been determined by Pt L_3 and Pd K edge extended X-ray absorption fine-structure spectroscopy. The bimetallic structure is confirmed from elemental line scans by scanning transmission electron microscopy of the individual 2-nm-sized particles. A general method is described to determine the surface composition of bimetallic nanoparticles even when both metals adsorb; for example, CO, by combining the quantitative characterization by X-ray absorption near-edge structure spectra at L edges with CO adsorption with the adsorption stoichiometry determined by Fourier transform infrared spectroscopy. Determination of the surface composition leads to a better understanding of the changes in catalytic chemistry that accompany alloy formation. Although monometallic Pt and Pd have similar turnover rates for neopentane hydrogenolysis and isomerization, on the basis of the surface composition, it appears that in the bimetallic PtPd catalysts, the rate and products are determined predominantly by Pt with little contribution from surface Pd. Density functional theory calculations indicate that the center of the Pt d-band density of states shifts to higher energy, or closer to the Fermi level, whereas that in Pd shifts to lower energy away from the Fermi level. Similarly, the calculated enthalpy of CO adsorption increases on Pt, but decreases on Pd. It is speculated that because of the very low surface coverage of the neopentane reaction intermediates, only surface atoms that form the strongest bonds are catalytically active—that is, Pt—rather than all surface atoms. The dominant role of Pd, therefore, appears to be to (slightly) modify Pt rather than to contribute to the catalytic conversion.

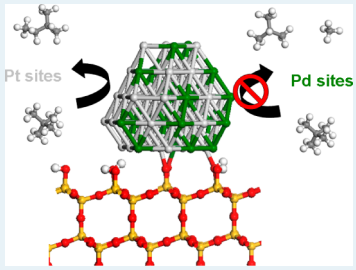

KEYWORDS: *PtPd bimetallic catalysts, neopentane hydrogenolysis and isomerization, bimetallic nanoparticle surface composition, L edge XANES of Pt, L edge XANES of Pd*

1. INTRODUCTION

Because of the electronic and chemical interaction between metals,[1−4] bimetallic catalysts often exhibit enhanced catalytic properties compared with simple mixtures of their monometallic counterparts.[5−8] Supported Pt−Pd nanoparticles are among the most widely studied and implemented bimetallic heterogeneous catalysts in important technological areas,[9] including aromatics hydrogenation,[10,11] petroleum hydrocracking,[12] emission control,[13] hydrogen storage,[14,15] and electrocatalysis in fuel cells.[16,17] Pt−Pd bimetallic nanocatalysts show not only enhanced selectivity and activity, but also better tolerance to poisons, such as sulfur.[10,18]

To fully understand the catalytic behavior, such as activity, selectivity, and stability, of a catalyst, the turnover rate (TOR), defined as the number of molecules converted per active surface atom per second, is an important metric. For catalysts with only one metal, or with two metals, but only one of which adsorbs a specific gas (e.g., CO), the TOR can be determined by chemisorption or infrared spectroscopy.[19−27] However, when both metals in a bimetallic catalyst adsorb CO, such as a PtPd catalyst, it is generally not possible to determine the surface composition of each metal. Combining quantitative characterization by XANES (X-ray absorption near-edge structure) spectra at L edges with CO adsorption with the

Special Issue: Operando and In Situ Studies of Catalysis

Received: July 9, 2012
Revised: October 8, 2012
Published: October 8, 2012

   dx.doi.org/10.1021/cs3004566 | ACS Catal. 2012, 2, 2433−2443

determination of the adsorption stoichiometry by FT-IR (Fourier transform infrared) spectroscopy, we present a general method for determination of the surface composition in bimetallic catalysts, even when both metals adsorb CO.

Neopentane hydrogenolysis is a widely used model reaction for characterization of noble metal catalysts. Because neopentane cannot form olefins or carbenium ions,[28] only metal-catalyzed reactions are possible. Neopentane reactions over bimetallic catalysts such as supported PtAu and PtSn have been studied.[29,30] For these catalysts, however, only Pt chemisorbs CO; thus, the number of active sites is readily determined. There are two main reaction pathways for this reaction: hydrogenolysis, or C−C bond cleavage to form methane and isobutane, and isomerization to form isopentane. The former reaction is generally undesirable, leading to light gas products. Isomerization is thought to occur by the C−C bond formation, followed by ring-opening of the strained cyclopropyl ring. The selectivity for ring closure in naphtha reforming is important for the production of aromatics from paraffins, whereas hydrogenolysis leads to liquid yield loss.[31−33] Thus, the properties, which lead to higher isomerization selectivity for neopentane, generally lead to higher aromatic selectivity for naphtha-reforming catalysts. The TOR and selectivity in the two reaction pathways of neopentane were determined for the monometallic Pt and Pd and two bimetallic PtPd nanoparticle catalysts. In addition, the Pt and Pd surface compositions were determined from the L_3 edge XANES with and without adsorbed CO and infrared spectroscopy. The comparison of the neopentane selectivities and TORs with the surface composition allows one to better determine the effect of alloy formation on catalytic performance.

2. EXPERIMENTAL AND COMPUTATIONAL METHODS

2.1. Catalyst Preparation. *2% Pt/SiO_2.* A 5 g portion of SiO_2 (Davisil silica gel from Sigma-Aldrich, 35−60 mesh, 200 m^2/g, and 1.15 mL/g pore volume) was added to 0.2 g of $Pt(NH_3)_4(NO_3)_2$ that was dissolved in 4 mL of water. About 1 mL of NH_4OH was added to adjust the pH to near 11. The solution was added dropwise to 5 g of silica while stirring and mixing. The impregnated mixture was dried at room temperature for 3 h then dried overnight at 125 °C and calcined at 225 °C in flowing air for 3 h. The calcined sample was reduced in 4% H_2/He at 250 °C. The elemental composition was determined to be 2.05% Pt by ICP analysis.

2.5% Pd/SiO_2. The same silica support was used, and strong electrostatic adsorption was the method of synthesis. Five grams of silica was stirred in 25 mL of water and concentrated ammonia to pH 11; 4.2 g of 10% $Pd(NH_3)_4(NO_3)_2$ in water solution was added rapidly while stirring.[34] After adsorption, the catalyst was filtered and washed with water twice and dried at room temperature for 3 h before it was dried overnight at 125 °C. The dried catalyst was reduced in 4% H_2/He at 250 °C. The metal loading was determined to be 2.56% Pd by ICP analysis.

1% Pd + 2% Pt/SiO_2. The same procedure of preparing the above Pt/SiO_2 catalyst was used. A 0.2 g portion of $Pt(NH_3)_4(NO_3)_2$ was dissolved in 3 mL of water then mixed with 1.4 g of 10% $Pd(NH_3)_4(NO_3)_2$ water solution. About 1 mL of NH_4OH was added to adjust the pH to 11. The solution was impregnated on 5 g of silica. The catalyst was dried at room temperature for 3 h, dried overnight at 125 °C, and calcined at 225 °C in flowing air for 3 h. The calcined sample was reduced in 4% H_2/He at 250 °C. The elemental composition of 1.07% Pd + 2.03% Pt was determined by ICP analysis. Following a similar synthesis procedure, a second bimetallic catalyst 0.75% Pd + 3% Pt/SiO_2 was prepared, and the elemental composition of 0.95% Pd + 3.69% Pt was determined by ICP analysis.

2.2. Characterization. *2.2.1. STEM and EDS.* Scanning transmission electron microscopy (STEM) was performed with an FEI Titan 80-300 operated at 300 kV. The FEI Titan is equipped with a CEOS GmbH double-hexapole aberration corrector for the probe-forming lens, which allows imaging with ∼0.1 nm resolution in the STEM mode. The images were acquired on high angle annular dark field with an inner collection angle of 52 mrad. Compositional analysis was performed using an EDAX Si (Li) energy dispersive spectroscopy (EDS) detector and FEI's TIA acquisition and analysis software. The STEM sample preparation involved mounting of powder samples on copper grids covered with lacey carbon support film and loading into the microscope. Before STEM characterization, the as-prepared samples were passivated with 0.1% O_2 in Ar and He for 3 h. For particle size measurements, we measured over 400 particles from several images of different areas of the catalyst, and the number average was calculated.

2.2.2. XAS Measurement. X-ray absorption spectroscopy (XAS) measurements for the Pd K (24 350 eV) and Pt L_3 (11 564 eV) edges were made on the insertion device beamline of the Materials Research Collaborative Access Team (MRCAT) at the Advanced Photon Source (APS), Argonne National Laboratory. Measurements were made in transmission mode. A platinum or palladium foil spectrum was acquired through a third ion chamber simultaneously with each measurement for energy calibration. Harmonic rejection was accomplished using a rhodium-coated or platinum-coated grazing incidence mirror for the Pd or Pt edges, respectively.

Catalyst samples were pressed into a cylindrical holder, which could simultaneously hold six samples, and placed into a controlled atmosphere cell equipped with shut-off valves to isolate the sample after pretreatment. The sample thickness was chosen to give a total absorbance (μx) at the Pt L_3 or Pd K edge between 1 and 2 absorption lengths and edge steps ($\Delta\mu x$) around 0.3−0.5. The catalysts were reduced at 250 °C at atmospheric pressure in 4% H_2/He at 50 cm^3/min flow rate. After reduction, the samples were purged with He at 100 cc/min and cooled to room temperature in He flow. Trace oxidants in He were removed by passing through a Matheson PUR-Gas Triple Purifier Cartridge. XAFS (X-ray absorption fine-structure) spectra were obtained at room temperature in He. Following data collection on the reduced catalysts, the samples were saturated for 5 min at 50 cm^3/min with 1% CO/He at room temperature, followed by a 5 min He purge. Additional XAS spectra of the Pt L_3 edge were obtained for the catalysts with adsorbed CO at room temperature.

XANES measurements for Pd L_3 (3173 eV) edges were made on the bending-magnet beamline of the X-ray Science Division (9-BM-B) at the APS. Measurements were made in fluorescence mode using a four-element silicon drift detector (SII NanoTechnology USA, Inc., Vortex-ME4). The region of interest was set in the detector electronics. Air absorption in the beam path was controlled by use of helium purging in the incident flight path. The in situ sample chamber, adapted on the basis of a design for an in situ grazing-incidence cell devised by Lee et al.,[35] was separated from the incident flight path by a 2.5-μm-thick aluminized mylar window.[36] The sample chamber was purged with a series of gases diluted to ∼4% in helium. The fluorescence window consisted of a 50-μm-thick piece of

dx.doi.org/10.1021/cs3004566 | ACS Catal. 2012, 2, 2433−2443

kapton, which served the function of blocking fluorescence from the silica supports (~10% transmission) while being much more transparent to Pd Lα fluorescence (~60% transmission). This allowed for acceptable signal-to-noise and mitigated count-rate limitations in the detector. The monochromator crystals were Si(111) with an energy resolution of ~0.35 eV at 3.1 keV. Harmonics were rejected by use of a Rh-coated flat mirror in the experimental station. The beam was focused to a spot size of ~1 mm in the horizontal and vertical directions by the use of a Rh-coated toroidal mirror. Energy calibration was achieved by the use of a Rh L_2 edge feature in I_0, which fell in the Pd pre-edge region.

Samples were pressed into self-supporting pellets in a steel holder configured for fluorescence measurements with a diameter of ~5 mm diameter at a 45° angle to the incoming beam. The catalysts were reduced at 250 °C at atmospheric pressure in 4% H_2/He at 50 cm^3/min. XANES spectra at the Pd L_3 (3173 eV) edges were taken after reduction. The reduced samples were cooled in 4% H_2/He to room temperature before they were exposed and saturated for 5 min at 50 cm^3/min with 1% CO/He at room temperature. Additional XANES spectra were obtained for the catalysts with adsorbed CO at room temperature.

2.2.3. Extended X-ray Absorption Fine-Structure (EXAFS) Data Analysis. Phase shift and backscattering amplitudes were obtained from the Pd and Pt foils for Pd−Pd and Pt−Pt scattering, respectively. For the experimental references, $\Delta\sigma^2$ was taken as 0.000. For Pt−Pd and Pd−Pt, phase and amplitude functions were calculated with FEFF.[37] S_0 and $\Delta\sigma^2$ were determined by fitting the single metal foils (Pt, 0.80 and 0.0045; Pd, 0.75 and 0.0055) that were used for calculation of the bimetallic scattering pairs. The bond distance was the average of the Pt−Pt (2.77 Å) and Pd−Pd (2.75 Å); that is, 2.76 Å. The PtPd and PdPt FEFF calculated χ's were used to prepare phase and amplitude functions for the bimetallic scattering pairs. The S_0 and $\Delta\sigma^2$ values of the FEFF calculated reference EXAFS were the same as for the metal foils. The phase and amplitude functions were determined from the theoretical χ's.

Standard procedures based on WINXAS 3.1 software were used to fit the XAS data. The EXAFS coordination parameters were obtained by a least-squares fit in k-space of the k^2-weighted Fourier transform data from 2.75 to 12.2 $Å^{-1}$, and the first shell fit of the magnitude and imaginary parts were performed between 1.6 and 3.2 Å. Because of the limited data range and number of allowed fit parameters of the two-shell fit in the bimetallic nanoparticles, the error in the fits was determined by fixing $\Delta\sigma^2$ at values typical of 2 nm nanoparticles, that is, 0.001−0.002 greater than metallic foils. The error in N was ±10% and in R was ±0.02 Å, within the typical fitting errors of EXAFS. The quality of the fits was equally good with both k^1 and k^3 weightings.

The normalized, energy-calibrated Pt (L_3) and Pd (K, L_3) edge XANES spectra were obtained by standard methods. The ΔXANES spectra were obtained by subtracting the normalized XANES spectrum of the catalyst in He from that with CO adsorption.

2.2.4. Diffuse Reflectance FTIR with CO Adsorption. Infrared spectra were obtained with an ABB Laboratory FTLA2000 FTIR spectrometer equipped with a Harrick Praying Mantis diffuse reflectance mode attachment and equipped with an environmental chamber. Each sample was crushed using a mortar and pestle and packed into the sample chamber. The chamber was purged with 4% H_2/N_2 (the total flow rate throughout the entire experiment was 100 cm^3/min), and the temperature was raised to 250 °C. After 30 min, the gas was purged with Ar while the temperature was maintained. After 10 min, the temperature was reduced to 25 °C. Next, a background scan was recorded, which was averaged over 64 scans with 4 cm^{-1} resolution. The sample was saturated with 1.6% CO/N_2 for 10 min, at which point the excess CO was purged with Ar for 15 min, and the final scan was recorded.

2.3. Catalytic Reaction of Neopentane. The neopentane hydrogenolysis reaction was studied using 0.05−0.1 g of catalyst diluted with 0.9 g of silica and loaded into a 0.5 in. o.d. quartz plug flow reactor. Glass wool and a 0.5 cm silica layer was used to support the catalyst bed of ~3 cm height. The reactor was purged with helium for about 5 min before each run, and the catalyst was reduced in 4% H_2/He as the temperature was increased to the reaction temperature, 271 ± 2 °C. A type K thermocouple was inserted from the bottom into the lower portion of the catalyst bed. Once the reaction temperature stabilized, the premixed reactant feed gas consisting of 0.35% neopentane and 3.5% H_2 balanced in He was flowed through the reactor system for 30 min to allow steady, stable operation. The flow rate of the feed gas was varied from 25 to 100 mL/min to obtain differential conversions between 0.5 and 6%. Each flow rate was run for at least an hour to ensure that steady state conversion for that flow had been reached. An Agilent 6890N gas chromatograph with an FID detector was used to analyze the products. The GC column was a J&W Scientific GS-Alumina column equipped with a back pressure regulator to hold the system at a constant pressure of 9 psi. Each experimental run was completed within 6 h for consistency. No appreciable deactivation was observed in any of the catalysts over this period of time. The relative error of the selectivity measurements was about 5% of the measured value. Turnover rates were calculated on the basis of the number of active sites determined by the dispersion (the dispersion was estimated as 1/particle diameter (nm)).[38] In the absence of catalyst, there was no conversion from the silica diluent.

2.4. Density Functional Theory Modeling. Density functional theory calculations were carried out using the Vienna Ab Initio Simulation Package (VASP).[39,40] A plane-wave basis set with a cutoff energy of 400 eV and projected augmented wave pseudopotentials[41,42] were used in all calculations. The Perdew−Burke−Ernzerhof (PBE−GGA) form of the correlation and exchange energy was used in all calculations. The (111) surfaces of Pd, Pt, and PdPt (whereby the fcc lattice with Pd−Pt bond distances was set at the average of monometallic bulk unit cells and was allowed to be optimized, shown in Supporting Information Figure S1) were cleaved to generate slabs with 6 layers. All calculations for 2 × 2 unit cells are carried out with a 5 × 5 × 1 Monkhorst Pack k-point grid.[43] Approximately four layers of vacuum separated the four-layer slabs in the z direction. The upper four layers of each surface were relaxed as well as all adsorbed CO molecules. A CO molecule was adsorbed onto each surface in the atop configuration. Geometries were judged to be optimized when the forces were within a convergence tolerance of 0.025 eV/Å. PDOS calculations were performed for the slabs using the default Wigner Seitz radii within VASP.

dx.doi.org/10.1021/cs3004566 | ACS Catal. 2012, 2, 2433−2443

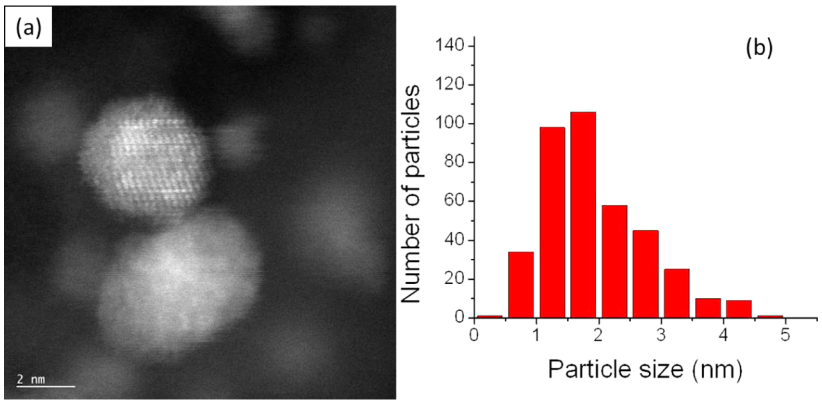

Figure 1. STEM images (a) and particle size distribution (b) for the 1% Pt + 2% Pd/SiO_2 catalyst.

3. RESULTS

3.1. Catalyst Characterization. The structure of the monometallic and bimetallic nanoparticle size and size distribution were determined using STEM imaging complemented by EDS. STEM images and the corresponding particle size distribution for the 1% Pt + 2% Pd/SiO_2 catalyst are shown in Figure 1a and b, respectively. The STEM images and size distributions for 2% Pt/SiO_2, 3% Pd/SiO_2, and 0.75% Pt + 3% Pd/SiO_2 catalysts are shown in Supporting Information Figure S2. The particle size distributions were estimated by measuring about 100−400 particles from several images of different areas on each catalyst. The average particle size and standard deviation for all four catalysts are listed in Table 1.

Table 1. Fit Parameters of the Fourier Transform of the First Shell of the k^2-Weighted EXAFS Spectra, and the Average Particle Size and Standard Deviation for All Four Catalysts[a]

sample and edge	scatter	N	R (Å)	$\Delta\sigma^2$ ($\times 10^{-3}$ Å^2)	E_0 (eV)	TEM size (nm)
2% Pt/SiO_2 at Pt L_3 edge	Pt−Pt	9.0	2.75	2.0	−1.4	1.7 ± 0.7[b]
2.5% Pd/SiO_2 at Pd K edge	Pd−Pd	6.8	2.74	2.0	−1.6	1.7 ± 0.3[b]
1% Pd + 2% Pt/SiO_2 at Pt L_3 edge	Pt−Pt	6.4	2.76	0.0	−0.4	1.9 ± 0.8
	Pt−Pd	4.3	2.75	0.0	8.9	
1% Pd + 2% Pt/SiO_2 at Pd K edge	Pd−Pd	4.6	2.74	1.0	−0.7	
	Pd−Pt	5.3	2.75	1.0	−1.8	
0.75% Pd + 3% Pt/SiO_2 at Pt L_3 edge	Pt−Pt	7.2	2.76	0.0	−0.5	1.9 ± 0.9
	Pt−Pd	3.0	2.75	0.0	8.6	
0.75% Pd + 3% Pt/SiO_2 at Pd K edge	Pd−Pd	3.3	2.74	1.0	−1.0	
	Pd−Pt	6.9	2.75	1.0	−2.2	

[a]Pt: Δk = 2.7−11.1 Å^{-1} and ΔR = 1.7−3.2 Å. Pd: Δk = 2.7−11.2 Å^{-1}; ΔR = 1.7−3.0 Å. ΔN = ±10%. R = ±0.02 Å. [b]Average size based on TEM and XAS.[44]

For bimetallic catalysts, the elemental distribution within the nanoparticles was determined by EDS. From Figure 2, it can be seen that in the 1% Pt + 2% Pd/SiO_2 catalyst, the particles generally show a uniform composition, although there was compositional variation from particle to particle (Supporting Information Table S1). There was less compositional variation from particle to particle for the 0.75% Pd + 3% Pt/SiO_2 catalyst (see Supporting Information Table S2). Although there is some variation in the particle compositions based on STEM and EDS, for both bimetallic catalysts, all particles contain both Pt and Pd.

Additional information on the PtPd particle structure and size was determined by EXAFS spectroscopy at the Pt L_3 and the Pd K edges. The typical quality of the EXAFS data is shown in Supporting Information Figure S3a and b for Pt and Pd, respectively. Figure 3 shows the magnitude of the Fourier transform, comparing catalysts PtPd/SiO_2 vs Pt/SiO_2 at the Pt L_3 edge and PtPd/SiO_2 vs Pd/SiO_2 at the Pd K edge, respectively, in Figure 3a and b. The figure shows that there are significant differences between the spectra of monometallic Pt or Pd and the bimetallic PtPd catalysts; that is, scattering other than Pt−Pt or Pd−Pd appears, indicating the formation of alloy in the PtPd catalyst. The fit parameters were determined by fitting both the magnitude and imaginary parts of the Fourier transform of the first shell of the k^2-weighted EXAFS spectra and are summarized in Table 1. Given that the EXAFS fit parameters are accurate to ∼10% and the elemental analysis is also accurate to ∼10%, we independently fit the coordination number and did not force them to any set value. For the sample with lower levels of Pd, although the error is slightly larger, the low coordination numbers are also within experimental uncertainty. A typical quality fit of the first-shell EXAFS data is shown in Supporting Information Figure S4a and b. Consistent with the results of STEM and EDS, XAS at both the Pt and Pd edges indicates that bimetallic nanoparticles are formed with approximately uniform composition of Pt and Pd.

3.2. FTIR with CO Adsorption on Catalysts. Figure 4 shows the FTIR spectra for Pt/SiO_2, Pd/SiO_2, and PtPd/SiO_2 with CO adsorption. The CO DRIFTS data for the Pt/SiO_2 catalyst shows two features in the spectrum. There is a large, sharp linear peak at 2071 cm^{-1} as well as a broader peak with much less intensity centered at 1810 cm^{-1} representing adsorption on bridging sites.[45−47] The Pd catalyst also had linear (2082 cm^{-1}) and bridging adsorption peaks (1945 cm^{-1}).[45,48,49] The bridging peak is much more pronounced than that on the Pt/SiO_2. The 1% Pd + 2% Pt catalyst also showed primarily linear CO adsorption (2073 cm^{-1}) positioned between the peaks of Pt/SiO_2 and Pd/SiO_2 and a small, broad feature centered at 1900 cm^{-1} representing the bridging adsorption.[50] Upon alloy formation, adsorption on both linear and bridging sites has less intensity compared with the absorption observed on single metal catalysts; especially, the

dx.doi.org/10.1021/cs3004566 | ACS Catal. 2012, 2, 2433−2443

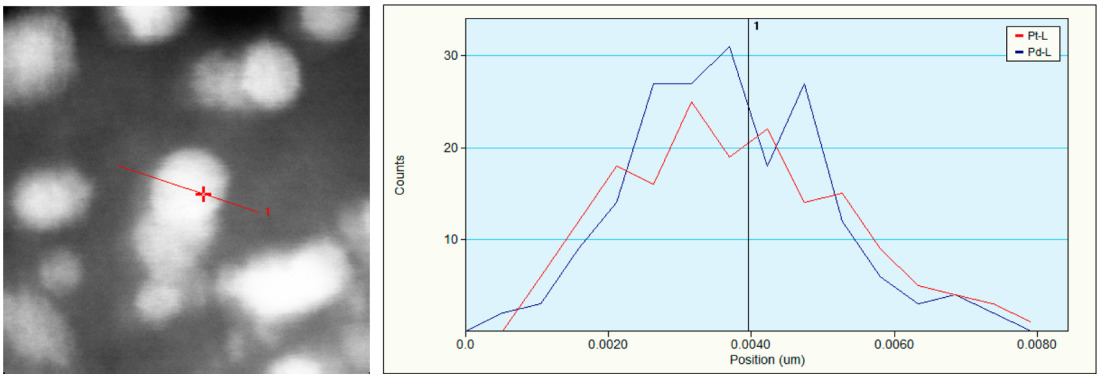

Figure 2. The EDS line scan and concentration profile for an individual particle in the 1% Pt + 2% Pd/SiO_2 catalyst; red line for Pt and blue line for Pd, respectively.

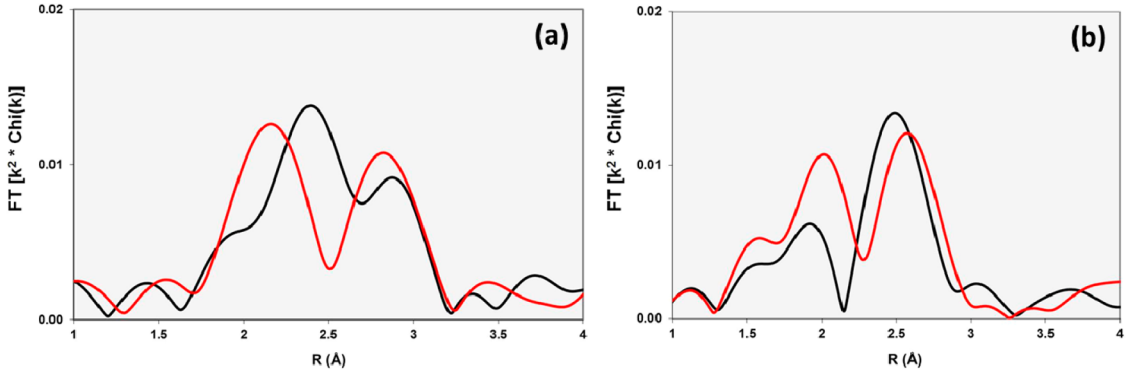

Figure 3. The magnitude of the Fourier transform comparing catalysts 1% Pd + 2% Pd/SiO_2 (red) vs Pt/SiO_2 (black) at the Pt L_3 edge Δk = 2.7−11.1 $Å^{-1}$ (a) and 1% Pd + 2% Pd/SiO_2 (red) vs Pd/SiO_2 (black) at the Pd K edge Δk = 2.7−11.2 $Å^{-1}$ (b).

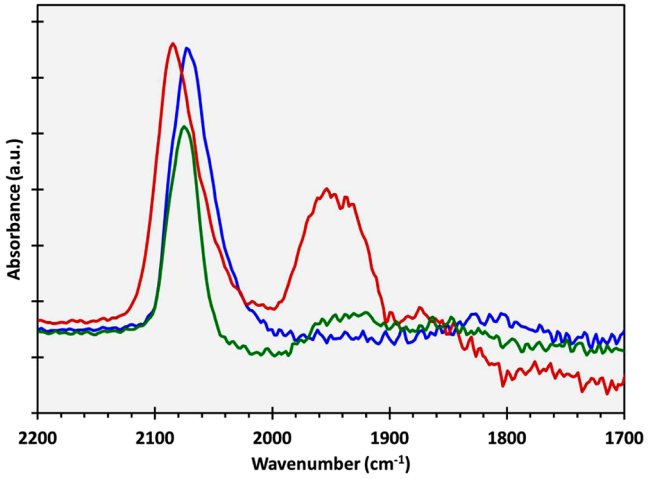

Figure 4. FT-IR spectra for Pt/SiO_2 (blue), Pd/SiO_2 (red), and PtPd/SiO_2 (green) with CO adsorption at room temperature.

bridging adsorption on alloy catalyst has dramatically less intensity than on Pd/SiO_2.

3.3. Pt and Pd L Edge XANES with CO Adsorption. Typically, the L_3 XANES spectra are used to determine the oxidation states or fraction of metallic and oxidized metal. In addition, changes in L_3 edge XANES spectra also occur with chemisorption of gases, for example, H_2 and CO.[51−55] Thus, such changes induced by chemisorption can be used to determine the type of adsorbate and its surface coverage. Adsorption of CO on Pt leads to significant changes in the position, intensity, and shape of the Pt L_3 XANES spectrum. Figure 5 shows the XANES spectra at the Pt L_3 edge for the Pt/SiO_2 before and after CO saturation. For the Pt L_3 edge, upon adsorption, there is a shift in the edge position to higher energy, ∼0.2 eV, as shown in the inset. In addition, there is an increase in whiteline intensity up to ∼10 eV above the edge for the Pt L_3

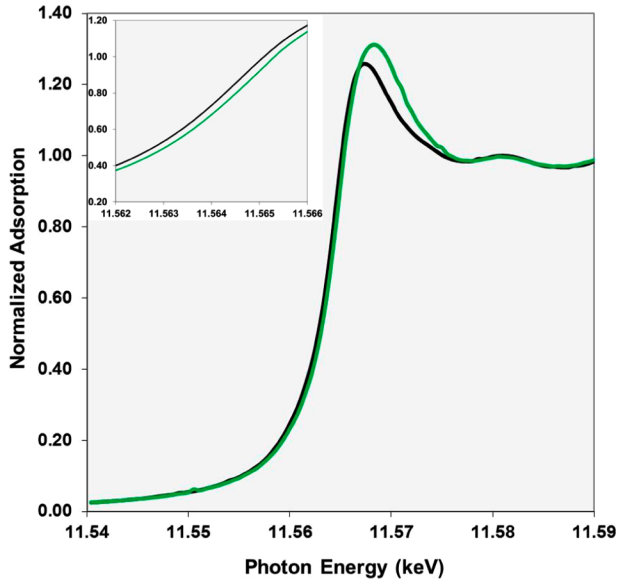

Figure 5. XANES spectra at the Pt L_3 edge from 11.54 to 11.59 keV for the Pt/SiO_2 without (black) and with (green) CO adsorption. The insert is a blow-up of the leading edge of the XANES spectra.

dx.doi.org/10.1021/cs3004566 | ACS Catal. 2012, 2, 2433−2443

edge. These changes are consistent with our previous work.[55] Figure 6 shows the XANES spectra at the Pd L_3 edges for the

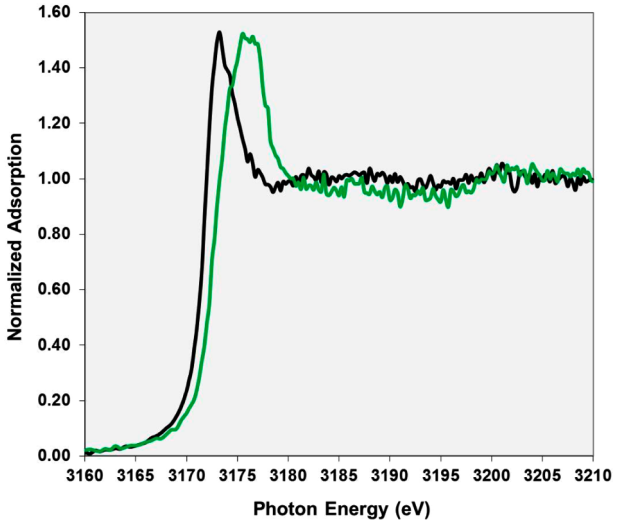

Figure 6. XANES spectra at the Pd L_3 edge from 3.16 to 3.21 keV for the Pd/SiO_2 without (black) and with (green) CO adsorption.

Pd/SiO_2 before and after CO saturation. There is a shift (~1 eV) in the edge position to higher energy upon adsorption and a slight broadening of the peak. Similar changes at the Pt L_3 and Pd L_3 are observed for the PdPt bimetallic catalysts, as shown in Supporting Information Figures S4 and S5.

If one subtracts the XANES in He from that with adsorbed CO, the difference (or ΔXANES) shows how the shape and intensity of the edge changes with adsorption of CO. Figure 7a and b shows the ΔXANES spectra of CO adsorption at the Pt L_3 edge for Pt/SiO_2 and 1% Pd + 2% Pt/SiO_2 and the Pd L_3 edge for Pd/SiO_2 and 1% Pd + 2% Pt/SiO_2, respectively. The CO ΔXANES at the Pt and Pd edges indicate that there are surface atoms of both elements. The decrease in intensity below the inflection point reflects a shift to higher energy at the edge, and the increase in the intensity above the inflection point is proportional to the increased intensity beyond the edge. It can be seen that the shape of the ΔXANES is very similar for the monometallic and bimetallic catalysts, and the spectra differ primarily in intensity. In the bimetallic $PtPd/SiO_2$, the magnitude of the ΔXANES decreases, corresponding to less adsorbed CO for both Pt and Pd. In general, these changes reflect differences in particle size, the fractional surface coverage, and the stoichiometry for adsorbed CO.

3.4. Neopentane Isomerization and Hydrogenolysis.

Neopentane hydrogenolysis has two possible reaction pathways, as shown in Figure 8: hydrogenolysis and isomerization. Hydrogenolysis involves a carbon−carbon bond cleavage and hydrogenation resulting in isobutane and methane.

Isomerization involves a ring closure/ring opening through a cyclopropyl intermediate to produce isopentane. As Figure 8 illustrates, the primary products are methane and isobutane for hydrogenolysis and isopentane for isomerization. In both cases, further reaction can occur to produce secondary products, such as propane and additional methane. Isomerization of the primary product, isopentane, can also lead to formation of *n*-pentane.

Figure 9 shows the selectivity plotted as a function of conversion for the 1% Pd + 2% Pt/SiO_2 catalyst. The data suggests that the reaction scheme proposed in Figure 8 is consistent with the data presented in Figure 9 because propane and ethane are not primary products, since the selectivity goes to zero as conversion goes to zero.[56] In contrast, isobutane, methane, and isopentane are clearly primary products because their selectivity is nonzero in the limit of zero conversion. Although *n*-pentane would not be expected to be a primary product, its selectivity is nonzero at zero conversion for the Pt-containing catalysts. The selectivities extrapolated to zero conversion are also given in Table 2. Although for Pt catalysts the initial isomerization product appears to undergo a second reaction (to *n*-pentane) before desorption, the initial hydrogenolysis product does not. At zero conversion, there is no selectivity to propane. For Pd, the reverse is true. There is no selectivity to *n*-pentane, but there is significant selectivity to propane and even ethane. In the bimetallic catalysts, the selectivity to *n*-pentane decreases with increasing Pd content; however, there is minimal selectivity to propane for either catalyst.

The isomerization selectivity of Pt was high at 0.64 (0.54 for isopentane plus 0.10 for *n*-pentane), but Pd was very low (0.05

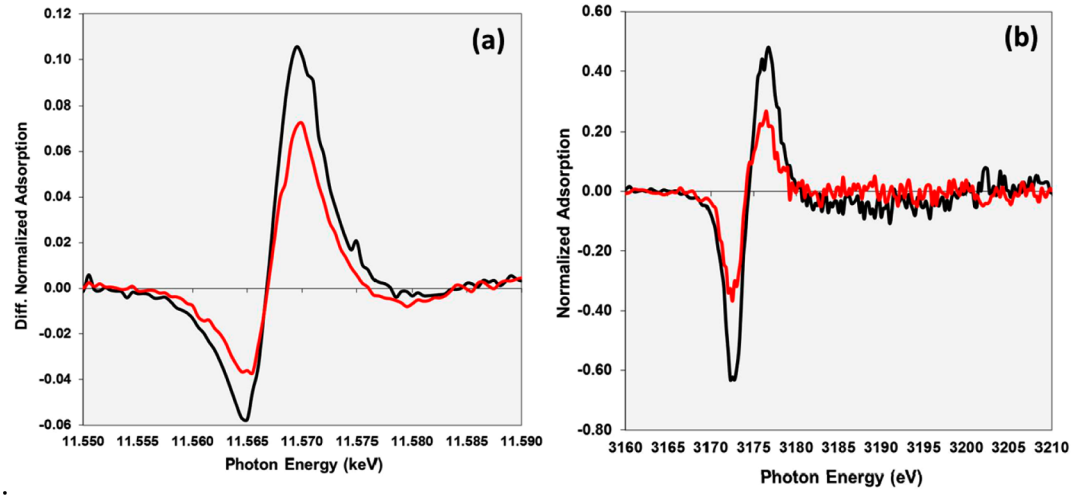

Figure 7. ΔXANES spectra of CO adsorption at (a) the Pt L_3 edge for Pt/SiO_2 and 1% Pd + 2% Pt/SiO_2 and (b) the Pd L_3 edge for 2.0 nm Pd/SiO_2 and 1% Pd + 2% Pt/SiO_2.

dx.doi.org/10.1021/cs3004566 | *ACS Catal.* 2012, 2, 2433−2443

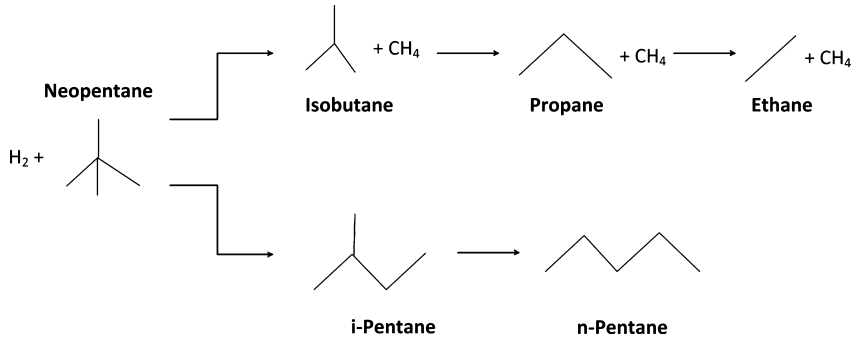

Figure 8. Neopentane hydrogenolysis reaction pathways: hydrogenolysis and isomerization.

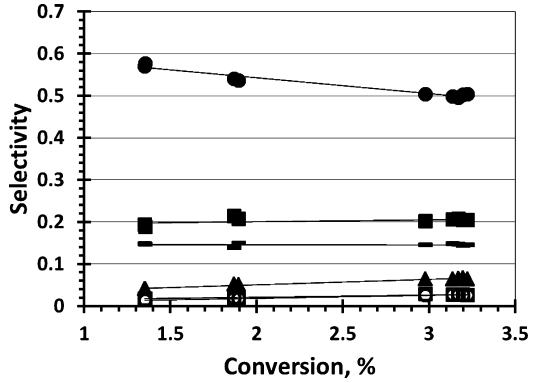

Figure 9. Selectivity vs conversion for the 1% Pd + 2% Pt/SiO_2 catalyst. Products: methane (■), ethane (□), propane (○), *i*-butane (−), isopentane (●), and *n*-pentane (▲).

isopentane and no *n*-pentane). The isomerization selectivity of the bimetallic PtPd catalysts was higher than either Pt or Pd alone. The total isomerization was ∼0.70 for both catalysts, whereas the selectivity to *n*-pentane increased with increasing Pt/Pd ratio, that is, 1% Pd + 2% Pt < 0.75% Pd + 3% Pt < Pt.

The turnover rates are also given in Table 2. The total number of atoms was determined from the composition, and the dispersion was calculated from the TEM average size.[57] In Table 2, the reported TOR for the bimetallic catalysts assumes that all surface atoms have the same TOR. The TOR of monometallic Pt is ∼1.8 times that of Pd. The TORs of the bimetallic PtPd catalysts are slightly lower than that of Pd and about half that of Pt.

3.5. Density Functional Theory (DFT): Energy of the d-Density of States (DOS) and CO Adsorption Energies. The projected density of states for Pd(111) vs Pd in PdPt(111) as well as Pt(111) vs PdPt(111) are compared in Figure 10. From the figure, one can see that the Pt d-bandwidth decreases in alloy relative to Pt(111), whereas the Pd d-bandwidth increases in the alloy as compared with Pd(111). The d-band centers of the top layer are affected by this change in width because the degree of filling for Pt and Pd changes only minimally when alloyed.[58] We find that the d-band center for Pd shifts away from the Fermi level (Pd(111) E_d = −1.76 eV; Pd in PdPt(111) E_d = −1.84 eV) when alloyed with Pt. Conversely, the d-band center of Pt shifts toward the Fermi level (Pt(111) E_d = −2.15 eV; Pt in PdPt(111) E_d = −2.05 eV).

Table 3 shows the effect of alloying on the binding energies of CO to the atop sites. A simple model is chosen to show how alloying affects the adsorption energy. At 0.25 ML coverage, CO adsorbs more strongly on atop sites on Pt(111) (−1.70 eV) than on Pd(111) sites (−1.50 eV). An enhanced behavior is seen on the alloy, which adsorbs CO stronger on Pt atop (−1.90 eV) than pure Pt and weaker on Pd atop (−1.39 eV) than the pure Pd. As we alloy Pt with Pd, the CO adsorption energy of Pd decreases, whereas the CO adsorption energy of Pt increases. The adsorption energy for CO in the atop site is used to demonstrate the changes in chemisorption energies due to alloy formation. Although the d-band center for Pd is closer to the Fermi level than that of Pt and, therefore, has a higher heat of adsorption than Pt, this is not true for atop adsorption of CO, because CO actually prefers the 3-fold hollow site on Pd.[59] However, this model is a simple demonstration that shows that upon alloy formation with Pt, Pd chemisorbs CO with a lower heat of adsorption than monometallic Pd. Calculations on other sites (bridge, fcc) show similar trends, thus it is not limited to atop coordination.

4. DISCUSSIONS

4.1. Surface Composition of the Alloy Catalyst. From STEM, EDS, and EXAFS, it has been confirmed that bimetallic nanoparticles have been synthesized. The TOR, however, was based on the dispersion assuming all atoms had equal rate and selectivity, rather than being based on the surface composition. Because both metals in the bimetallic catalysts adsorb CO, for example, chemisorption and FT-IR cannot be used to determine the numbers of surface atoms for each metal. The advantage of XANES spectroscopy is that it is specific only to the amount of CO adsorbed on one metal and is essentially independent of the amount of CO adsorbed by the second metal. Adsorption of CO on Pt and Pd leads to a shift in the

Table 2. Neopentane Turnover Rates (TOR) and Reaction Products Extrapolated to 0% Conversion at 271 °C

			initial product distribution (%)					
catalyst	dispersion	TOR (mol conv/metal site/s)	CH_4	C_2H_6	C_3H_8	C_4H_{10}	i-C_5H_{12}	n-C_5H_{12}
2.06% Pt/SiO_2	0.57	1.3×10^{-3}	18	0	0	18	54	10
2.56% Pd/SiO_2	0.57	7.3×10^{-4}	53	1	9	32	5	0
0.75% Pd + 3% Pt/SiO_2	0.51	6.5×10^{-4}	16	1	1	14	62	8
1% Pd + 2% Pt/SiO_2	0.51	5.2×10^{-4}	16	2	1	13	68	2

dx.doi.org/10.1021/cs3004566 | ACS Catal. 2012, 2, 2433−2443

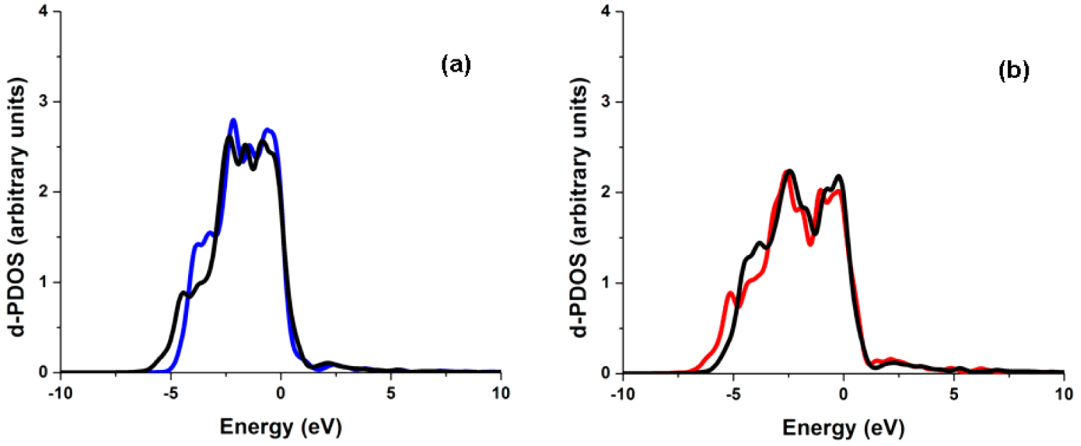

Figure 10. Projected density of states for the (a) Pd(111) (blue) vs Pd in PtPd(111) (black) and (b) Pt(111) (red) vs Pt in PdPt(111) (black).

Table 3. Energies of Adsorption of Atop CO at 0.25 ML Coverage

surface	E_{ads} (eV)
Pt(111)	−1.70
Pd(111)	−1.50
PdPt(111)	−1.39 (Pd)
	−1.90 (Pt)

edge energy and change in the shape of the XANES, as shown in Figures 5 and 6. These changes (ΔXANES) are proportional to the amount of adsorbed CO.[54,55] Because CO saturates the surface of Pt and Pd nanoparticles at room temperature, the ΔXANES can be calibrated, for example, with a single metal particle of known size to determine the surface composition for that specific atom, for example, Pt or Pd, in a bimetallic nanoparticle.

Figure 7a shows the Pt L_3 edge ΔXANES spectra of CO adsorption at room temperature for 2% Pt/SiO_2 and 1% Pt + 2% Pd/SiO_2, respectively. Using the ΔXANES spectrum for Pt/SiO_2 as the reference, the relative fraction of CO adsorption on Pt atoms in the PdPd bimetallic catalyst can be determined, that is, the intensity ratio of ΔXANES (PtPd) over ΔXANES (Pt). The surface CO coverage on $PtPd/SiO_2$ is ∼70% of coverage on Pt/SiO_2, which is determined by fitting the ΔXANES in the PtPd with that of the Pt only. The repeatability of the ΔXANES fit is ∼5%. In general, the ΔXANES fit also has to be corrected for any differences in particle size or dispersion, which can be determined by TEM and CO adsorption stoichiometry, which is determined from the IR spectra. For example, if there were an increase in size in the bimetallic NP, there would be a decrease in the ΔXANES just due to the lower fraction of surface atoms. The decrease is proportional to the ratio of the dispersions of the two catalysts. From TEM, the differences in particle size and dispersion of monometallic Pt and 1% Pt + 2% Pd/SiO_2 are small: 1.9 and 1.7, respectively. Correcting for this size (0.70 × 1.7/1.9) gives a Pt surface fraction of 0.63. In addition, from the FT-IR (Figure 4), both catalysts have primarily linearly adsorbed CO. Therefore, the surface composition of Pt atoms on $PtPd/SiO_2$ is unchanged, ∼65%.

From the Pd L_3 edge, shown in Figure 7b, the fit of the ΔXANES of CO on $PtPd/SiO_2$ is ∼50% that on Pd/SiO_2. The Pd/SiO_2 used to determine the ΔXANES was very similar in size to that of the bimetallic $PtPd/SiO_2$ catalysts. Correcting for the difference in size of Pd/SiO_2 to $PtPd/SiO_2$ (1.7/1.9), the Pd surface coverage is 0.45. However, on Pd/SiO_2, there is a significant amount of bridging CO, with a 1.33 Pd/CO ratio;[19] whereas on the bimetallic catalyst, CO is bound in primarily a linear configuration with little bridging CO. Accounting for this difference, the surface composition of Pd atoms on $PtPd/SiO_2$ is ∼0.33 (0.45/1.33).

Although there are uncertainties in the determination of the average TEM particle size, M/CO ratio by IR spectra and ΔXANES fits, the relative error is common to both the monometallic and bimetallic NP's. Determination of the metallic surface coverage by taking the ratio of these measurements leads to small errors in the composition of the surface coverage, typically less than ∼10%, as evidenced by the agreement of the fraction of Pt and Pd in 1% Pt + 2% Pd/SiO_2 determined independently from both the Pt and Pd L edges. The sum of surface composition of Pt and Pd atoms (∼65% Pt atoms and ∼35% Pd atoms) is very close to 1.0 within reasonable uncertainty of the XANES, IR, TEM, and EXAFS measurements. The Pt surface composition determined from the L_3 XANES for the 0.75% Pd + 3% Pt/SiO_2 catalyst was determined to be ∼80% Pt. For this catalyst, the Pd L edge ΔXANES was not measured, but from the Pt surface composition, the fraction of Pd atoms would be around 20%.

There are several assumptions and limitations of the described method. First, the method assumes that there is saturation adsorption. Although this is likely for Pt and Pd, it may not be true for all metals, such as Au, Ag, Cu, and others. For these metals, alternative adsorbates will be required. Second, the method also assumes that the surface composition is not changed by the adsorbate. The EXAFS of these PtPd nanoparticles was identical, suggesting that this is true for these catalysts; however, chemisorption of oxygen, for example, does often lead to changes in the surface composition.[60] In addition, even CO can act to segregate metals whose affinity for CO differs substantially from one another.[61] Thus, although the fraction of oxidized surface atoms can be determined, this may be different from that in the reduced catalyst. In addition, the method relies on the ability to determine the difference in the XANES spectra with and without adsorbate. This is generally possible for nanoparticle sizes of less than ∼10 nm. For larger particles, the fraction of surface atoms is too small to measure the amount of surface atoms (with adsorbate) reliably.

In the determination of the Pd surface fraction in the $PtPd/SiO_2$ catalysts, the Pd CO stoichiometry was assumed to be the

dx.doi.org/10.1021/cs3004566 | ACS Catal. 2012, 2, 2433−2443

same as that for Pt, for example, all linear bonding. The correctness of this assumption affects the Pd surface coverage (determined from the Pd edge). If the IR in the bimetallic is assumed to be identical to that in the monometallic NP, then the Pd surface coverage would be 0.45, which does not agree with the value determined from the Pt edge. Although the Pd/CO ratio cannot be independently determined, the high fraction of linear Pd CO bonding likely results from the low Pd surface coverage. Thus, the high fraction of Pt neighbors leads to few Pd−Pd for CO bridge bonding. For Pd bimetallic nanoparticles with a high fraction of Pd, the Pd/CO ratio may be more similar to that in the monometallic Pd. Whereas the stoichiometry of CO bonding adds to the uncertainty of the surface coverage measurements, other metals often have M/CO ratios near unity; thus, this becomes less of a problem.

4.2. Correlation between Surface Composition and Catalytic Behavior. The turnover frequencies of the bimetallic catalysts reported in Table 2 were based on the fraction of total surface atoms, independent of surface composition, and were lower than both monometallic catalysts. Because the TOR of the PtPd catalysts was only slightly lower than monometallic Pd, one might conclude that the surface has a high fraction of Pd atoms. However, for the 1% Pd + 2% Pt/SiO_2, the fraction of surface Pt atoms is ~0.65. If the TOR of Pt and Pd were unchanged in the bimetallic catalyst, the experimental TOR would be intermediate between that of Pt and Pd; however, the TOR is 0.4 times that of Pt and 0.71 times that of Pd. In other words, the experimental TOR is much lower than the TOR predicted using the monometallic rates and fraction of surface atoms. Similarly, if the TORs of Pt and Pd on 0.75% Pd + 3% Pt (0.80 surface Pt) were identical to that in the monometallic Pt and Pd, the expected TOR would be also between that of Pt and Pd; however, the experimental TOR that is 0.5 times that of Pt and 0.9 times that of Pd. For both catalysts, the experimental TOR is lower than the expected value from the surface composition.

The neopentane isomerization selectivity in both PtPd bimetallic catalysts is slightly higher, 0.7, than for Pt, 0.64, and much higher than Pd, 0.05. Without knowledge of the surface composition, one might conclude that there is a high Pt surface coverage. Using the estimated surface coverages and the TOF of the pure metals, one can estimate that the kinetic averaged selectivity, for example, for isomerization, which is the isomerization rate of the surface atoms divided by the total rate. For 1% Pt + 2% Pd, the kinetic average selectivity is 0.50. This selectivity is intermediate between that of Pt and Pd. Similarly, the kinetic averaged isomerization selectivity of the 0.75% Pd + 3% Pt catalyst (0.80 Pt + 0.20 Pd surface composition) is 0.55. The experimental values of 0.70 and 0.71 are significantly higher than both of these calculations and even higher than that for monometallic Pt. Thus, although the bimetallic catalysts have TORs that are lower than the monometallic catalysts, the selectivity is significantly higher than the kinetic average of the surface atoms based on the monometallic rates and selectivities.

It was previously noted that although *n*-pentane is not an expected primary product in the isomerization pathway, nevertheless, there were low selectivities (extrapolated to zero conversion) to this product for the Pt containing catalysts. The *n*-pentane selectivities were 10%, 8%, and 2% for Pt, 0.75% Pd + 3% Pt, and 1% Pd + 2% Pt, respectively. The selectivity of *n*-pentane was 0% for monometallic Pd. The most probable reaction pathway for *n*-pentane production involves a second isomerization step prior to isopentane desorption. The increase in the selectivity to *n*-pentane selectivity can be correlated with the increase in surface coverage of Pt, as seen in Figure 11. This

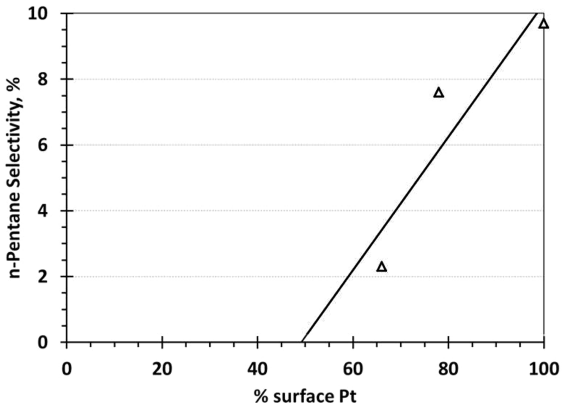

Figure 11. *n*-Pentane selectivity vs the fractional surface composition of Pt atoms.

correlation may imply that isomerization to *n*-pentane requires multisite Pt−adsorbate bond formation (whereas isomerization to isopentane may not), and the addition of Pd to the surface breaks up some of these adjacent Pt sites.

The selectivity and TORs determined from the surface composition show that mixing Pt and Pd does not result in just an additive effect of the two separate metals. The TOR is lower than the monometallic rates, but the bimetallic isomerization selectivity is higher than the monometallic catalysts.

4.3. Correlation between Simulation and Experimental Results. Norskov and many others have previously used the location of the d-band as a critical descriptor of catalytic performance.[6,58,62−67] From the results in Figure 10, the results show that reactivity (and CO binding energy) of Pd decreases in the alloy while Pt increases. This is not intuitively obvious. Naively, one could suppose that the Pd in a PdPt alloy is in expansion because the lattice constant of PdPt is larger than for plain Pd, as mentioned above.[6] However, this would result in a narrowing of Pd PDOS. Conversely, one could conjecture that Pt would respond as if it were in compression (and its d-band would expand). The observed behavior results from the fact that Pt has a larger extent, that is, spatially larger d orbitals, than Pd.[68] This implies that in the alloy, Pd is now "overbonded" by Pt and experiences increased hybridization due to the larger overlap with Pt than it would have had with its Pd neighbors. Similarly, Pt is now "underbonded" by Pd since the d orbitals of Pd do not extend as far as Pt. These differences in extent are manifested by the large increase in the melting temperature of Pt (1768 °C) with respect to Pd (1555 °C).[69]

In addition, from our simple model of CO adsorption, we observe that the behavior of the alloy surface is not merely an average of the monometallic surfaces. Both the DFT calculations of CO adsorption and our catalytic turnover rates and selectivity for neopentane hydrogenolysis/isomerization suggest that the bimetallic PtPd catalysts are unique and display behavior different from those of the monometallic catalysts. This behavior has been predicted for other alloy systems because of synergistic combinations of strain and ligand effects.[70] If the alloy catalyst possessed behavior that was simply an additive behavior of its two parts, then we would expect that the activity of the catalyst would lie between Pt and Pd and that the selectivity would also lie between Pt and Pd. Of

dx.doi.org/10.1021/cs3004566 | ACS Catal. 2012, 2, 2433−2443

course, this is not what we observe. Instead, both the activity and selectivity lie outside of the range defined by the monometallic catalysts. It appears that neopentane conversion has been significantly turned off on Pd surface sites, which predominately yield hydrogenolysis. Like CO, it appears that perhaps neopentane adsorption (and activation) is weakened on Pd sites in the alloy. In effect, the alloy catalyst now operates as if only Pt is present, and the reactivity and selectivity appears to be completely governed by the catalytic conversion on Pt sites in the alloy. If only Pt sites are catalytic, then the observed TOR in the bimetallic nanoparticles is only slightly lower than that in monometallic Pt. The lower rate per total surface atoms suggests that one can ignore the Pd sites entirely in the alloy when predicting the rate. We can further speculate from the IR data that few hollow or bridging Pd sites exist in the alloy surface. This implies that an additional effect of alloying is the disruption of these sites where the molecule can experience high coordination with surface Pd that lead to hydrogenolysis.[71] In contrast, adsorption of neopentane to active sites on Pt may follow the example of CO adsorption, for which atop sites are desirable.[72]

If only surface Pt is active, as suggested, the isomerization selectivity is also very similar to that of monometallic Pt. The role of Pd, therefore, is to slightly modify the Pt d-DOS, leading to a small but significant enhancement in isomerization selectivity. Although the reactivity of alloys of disparate metals (e.g., PtSn,[73] PdAg[74]) have often been described as merely modification of the active metal, this behavior seems unusual (and unexpected) for PtPd, in which the metals are similar in electronic structure.

5. CONCLUSION

A method for determination of the surface composition in bimetallic nanoparticles is given even for alloys in which both metals adsorb, for example, CO. By measuring the change in the L_3 edge XANES spectra with and without CO in bimetallic particles and comparing these changes with those in monometallic particles of known size along with the stoichiometry for CO adsorption, the fraction of surface atoms can be determined.

Determination of the surface coverage allows one to study the effects of alloy formation on TOR and selectivity for a given reaction, for example, neopentane hydrogenolysis. For PtPd bimetallic nanoparticles, the TORs are lower than that expected from the Pt and Pd surface composition, whereas the neopentane isomerization selectivity is higher. In addition, the isomerization selectivity to *n*-pentane (extrapolated to zero conversion) increases with the Pt surface coverage above ~50%. Density functional theory calculations indicate the Pt d-DOS shifts to higher energy, which leads to an increase in the adsorption enthalpy of CO. For Pd, the d-DOS shifts to lower energy, and the Pd-CO bond energy decreases. Although there are changes in the DOS for both Pt and Pd, these are only slightly altered compared with the monometallic nanoparticles, implying that the catalytic properties are only slightly changed. The neopentane TOR's and selectivities of the PtPd bimetallic catalysts can be rationalized by assuming that the surface coverage of reaction intermediates is low and only sites forming the strongest bonds affect conversion. Thus, even though Pt and Pd monometallic nanoparticles have similar TOR's, in the bimetallic PtPd, Pt atoms appear to dominate the catalytic conversion. TOR's based on only surface Pt are slightly smaller than that in monometallic Pt, and the selectivity is slightly higher. Thus, Pd appears to act as a Pt promoter and have little catalytic activity of its own. In general, the ability to determine the surface composition will allow for a better understanding of the spectroscopic and catalytic properties of bimetallic nanoparticle catalysts.

■ ASSOCIATED CONTENT

Supporting Information

Additional figures showing TEM and XAS of additional samples is provided. This material is available free of charge via the Internet at http://pubs.acs.org.

■ AUTHOR INFORMATION

Corresponding Author

*E-mails: (R.J.M.) rjm@uic.edu, (J.T.M.) millerjt@anl.gov.

Notes

The authors declare no competing financial interest.

■ ACKNOWLEDGMENTS

This material is based upon work supported as part of the Institute for Atom-Efficient Chemical Transformations (IACT), an Energy Frontier Research Center funded by the U.S. Department of Energy, Office of Science, Office of Basic Energy Sciences. R.J.M., C.G., and D.C. gratefully acknowledge funding for this work from the National Science Foundation (CBET Grant No. 0747646). We gratefully acknowledge LCRC at Argonne National Lab for allocation grant intermetallic, which was used to perform most of the calculations described herein. The STEM and EDS work was performed in the Environmental Molecular Sciences Laboratory, a national scientific user facility sponsored by the U.S. Department of Energy's Office of Biological and Environmental Research, located at Pacific Northwest National Laboratory (PNNL) in Richland, WA. Use of the Center for Nanoscale Materials was supported by the U.S. Department of Energy, Office of Science, Office of Basic Energy Sciences, under Contract No. DE-AC02-06CH11357. The work was supported by the National Advanced Biofuels Consortium, which is funded by the Department of Energy's Office of Biomass Program with recovery act funds. Use of the Advanced Photon Source was supported by the U.S. Department of Energy, Office of Science, Office of Basic Energy Sciences, under Contract No. DE-AC02-06CH11357. MRCAT operations are supported by the Department of Energy and the MRCAT member institutions. Use of the 9 μ_B beamline at the Advanced Photon Source, an Office of Science User Facility operated for the U.S. Department of Energy (DOE) Office of Science by Argonne National Laboratory, was supported by the U.S. DOE under Contract No. DE-AC02-06CH11357.

■ REFERENCES

(1) Rodriguez, J. A. *Surf. Sci. Rep.* **1996**, *24*, 223.
(2) Rodriguez, J.; Goodman, D. W. *J. Phys. Chem.* **1991**, *95*, 4196.
(3) Rodriguez, J. A.; Goodman, D. W. *Science* **1992**, *257*, 897.
(4) Rodriguez, J. A.; Kuhn, M. *J. Chem. Phys.* **1995**, *102*, 4279.
(5) Chen, M. S.; Kumar, D.; Yi, C. W.; Goodman, D. W. *Science* **2005**, *310*, 291.
(6) Kitchin, J. R.; Norskov, J. K.; Barteau, M.; Chen, J. G. *Phys. Rev. Lett* . **2004**, *93*, 156801.
(7) Campbell, C. T. *Annu. Rev. Phys. Chem.* **1990**, *41*, 775.
(8) Toshima, N.; Yonezawa, T. *New J. Chem.* **1998**, *22*, 1179.
(9) Tao, F.; Grass, M. E.; Zhang, Y.; Butcher, D. R.; Renzas, J. R.; Liu, Z.; Chung, J. Y.; Mun, B. S.; Salmeron, M.; Somorjai, G. A. *Science* **2008**, *322*, 932.

(10) Navarro, R. M.; Pawelec, B.; Trejo, J. M.; Mariscal, R.; Fierro, J. L. G. *J. Catal.* **2000**, *189*, 184.
(11) Barrio, V. L.; Arias, P. L.; Cambra, J. F.; Güemez, M. B.; Pawelec, B.; Fierro, J. L. G. *Fuel* **2003**, *82*, 501.
(12) Fiermans, L.; De Gryse, R.; De Doncker, G.; Jacobs, P. A.; Martens, J. A. *J. Catal.* **2000**, *193*, 108.
(13) Roy, S.; Baiker, A. *Chem. Rev.* **2009**, *109*, 4054.
(14) Kobayashi, H.; Yamauchi, M.; Kitagawa, H.; Kubota, Y.; Kato, K.; Takata, M. *J. Am. Chem. Soc.* **2010**, *132*, 5576.
(15) Kobayashi, H.; Yamauchi, M.; Kitagawa, H.; Kubota, Y.; Kato, K.; Takata, M. *J. Am. Chem. Soc.* **2008**, *130*, 1818.
(16) Peng, Z. M.; Yang, H. *J. Am. Chem. Soc.* **2009**, *131*, 7542.
(17) Lim, B.; Jiang, M. J.; Camargo, P. H. C.; Cho, E. C.; Tao, J.; Lu, X.; Zhu, Y.; Xia, Y. *Science* **2009**, *324*, 1302.
(18) Yasuda, H.; Yoshimura, Y. *Catal. Lett.* **1997**, *46*, 43.
(19) Palazov, A.; Chang, C. C.; Kokes, R. J. *J. Catal.* **1975**, *36*, 338.
(20) Palazov, A.; Bonev, C.; Kadinov, G.; Shopov, D.; Lietz, G.; Völter, J. *J. Catal.* **1981**, *71*, 1.
(21) Bastein, A. G. T. M.; Toolenaar, F. J. C. M.; Ponec, V. *J. Catal.* **1984**, *90*, 88.
(22) Palazov, A.; Bonev, C.; Shopov, D.; Lietz, G.; Sárkány, A.; Völter, J. *J. Catal.* **1987**, *103*, 249.
(23) Balakrishnan, K.; Sachdev, A.; Schwank, J. *J. Catal.* **1990**, *121*, 441.
(24) Liu, R.; Tesche, B.; Knözinger, H. *J. Catal.* **1991**, *129*, 402.
(25) Hwang, C.; Woo, S. I. *Stud. Surf. Sci. Catal.* **1994**, *83*, 339.
(26) Skoda, F.; Astier, M. P.; M., P. G.; Primet, M. *Catal. Lett.* **1994**, *29*, 159.
(27) de Menorval, L. C.; Chaqroune, A.; Coq, B.; Figueras, F. *Faraday Trans.* **1997**, *93*, 3715.
(28) Juszczyk, W.; Karpinski, Z. *J. Catal.* **1989**, *117*, 519.
(29) Balakrishnan, K.; Schwank, J. *J. Catal.* **1991**, *132*, 451.
(30) Balakrishnan, K.; Schwank, J. *J. Catal.* **1991**, *127*, 287.
(31) Akhmedov, V. M.; Al-Khowaiter, S. H. *Catal. Rev. Sci. Eng.* **2007**, *49*, 33.
(32) Ciapetta, F. G.; Wallace, D. N. *Catal. Rev.* **1972**, *5*, 67.
(33) Aitani, A. Reforming Processes. In *Catalytic Naphtha Reforming*, 1st ed.; Antos, G. J., Aitani, A. M., Parera, J. M., Eds.; Marcel Dekker: New York, 1995; p 415.
(34) Miller, J. T.; Schreier, M.; Kropf, A. J.; Regalbuto, J. R. *J. Catal.* **2004**, *225*, 203.
(35) Lee, S.; Lee, B.; Seifert, S.; Vajda, S.; Winans, R. E. *Nucl. Instrum. Methods Phys. Res., Sect. A* **2011**, *649*, 200.
(36) Bolin, T.; Wu, T.; Schweitzer, N.; Lobo, R.; Kropf, A. J.; Wang, H.; Hu, Y.; Miller, J. T.; Heald, S. *Catal. Today* **2012**, submitted.
(37) Rehr, J. J.; Mustre de Leon, J.; Zabinsky, S. I.; Albers, R. C. *J. Am. Chem. Soc.* **1991**, *113*, 5135.
(38) Williams, W. D.; Shekhar, M.; Lee, W. S.; Kispersky, V.; Delgass, W. N.; Ribeiro, F. H.; Kim, S. M.; Stach, E. A.; Miller, J. T.; Allard, L. F. *J. Am. Chem. Soc.* **2010**, *132*, 14018.
(39) Kresse, G.; Furthmuller, J. *Phys. Rev. B* **1996**, *54*, 11169.
(40) Kresse, G.; Furthmuller, J. *Comput. Mater. Sci.* **1996**, *6*, 15.
(41) Blochl, P. E. *Phys. Rev. B* **1994**, *50*, 17953.
(42) Kresse, G.; Joubert, D. *Phys. Rev. B* **1999**, *59*, 1758.
(43) Monkhorst, H. J.; Pack, J. D. *Phys. Rev. B* **1976**, *13*, 5188.
(44) Miller, J. T.; Kropf, A. J.; Zha, Y.; Regalbuto, J. R.; Delannoy, L.; Louis, C.; Bus, E.; van Bokhoven, J. A. *J. Catal.* **2006**, *240*, 222.
(45) Eischens, R. P.; Francis, S. A.; Pliskin, W. A. *J. Phys. Chem.* **1956**, *60*, 194.
(46) Crossley, A.; King, D. A. *Surf. Sci.* **1980**, *95*, 131.
(47) Heyden, B. E.; Bradshaw, A. M. *Surf. Sci.* **1983**, *125*, 787.
(48) Sheppard, N.; Nguyen, T. T. *Adv. Infrared Raman Spectrosc.* **1978**, 5.
(49) Gelin, P.; Sedle, A. R.; Yates, J. T. J. *J. Phys. Chem.* **1984**, *88*, 2978.
(50) Todoroki, N.; Osano, H.; Maeyama, T.; Yoshida, H.; Wadayama, T. *Appl. Surf. Sci.* **2009**, *256*, 943.
(51) Ankudinov, A. L.; Rehr, J. J.; Low, J.; Bare, S. R. *Phys. Rev. Lett* . **2001**, *86*, 1642.
(52) Stakheev, A. Y.; Zhang, Y.; Ivanov, A. V.; Baeva, G. N.; Ramaker, D. E.; Koningsberger, D. C. *J. Phys. Chem. C* **2007**, *111*, 3938.
(53) Oudenhuijzen, M. K.; van Bokhoven, J. A.; Miller, J. T.; Ramaker, D. E.; Koningsberger, D. C. *J. Am. Chem. Soc.* **2005**, *127*, 1530.
(54) Guo, N.; Fingland, B. R.; Williams, W. D.; Kispersky, V. F.; Jelic, J.; Delgass, W. N.; Ribeiro, F. H.; Meyer, R. J.; Miller, J. T. *Phys. Chem. Chem. Phys.* **2010**, *12*, 5678.
(55) Lei, Y.; Jelic, J.; Nitsche, L.; Meyer, R. J.; Miller, J. T. *Top. Catal.* **2011**, *54*, 334.
(56) Bhore, N. A.; Klein, M. T.; Bischoff, K. B. *Chem. Eng. Sci.* **1990**, *45*, 2109.
(57) Characterization of Solid Catalysts. In *Handbook of Heterogeneous Catalysis*, 2nd ed.; Ertl, G. H. K., Schüth, F., Weitkamp, J., Eds.; Wiley-VCH: Weinheim, 2008; Vol. 2, p 439.
(58) Kitchin, J. R.; Norskov, J. K.; Barteau, M. A.; Chen, J. G. *J. Chem. Phys.* **2004**, *120*, 10240.
(59) Hoffmann, F. M. *Surf. Sci. Rep.* **1983**, *3*, 109.
(60) Menning, C. A.; Hwu, H. H.; Chen, J. G. G. *J. Phys. Chem. B* **2006**, *110*, 15471.
(61) Gao, F.; Wang, Y. L.; Goodman, D. W. *J. Phys. Chem. C* **2009**, *113*, 14993.
(62) Greeley, J.; Norskov, J. K. *Surf. Sci.* **2005**, *592*, 104.
(63) Hammer, B.; Norskov, J. K. Theory of Adsorption and Surface Reactions. In *Chemisorption and Reactivity on Supported Clusters and Thin Films*; Lambert, R. M., Pacchioni, G., Eds.; Kluwer Academic Publishers: Dordrecht, The Netherlands, 1997; p 285.
(64) Hammer, B.; Norskov, J. K. *Nature* **1995**, *376*, 238.
(65) Jacobsen, C. J. H.; Dahl, S.; Clausen, B. S.; Bahn, S.; Logadottir, A.; Norskov, J. K. *J. Am. Chem. Soc.* **2001**, *123*, 8404.
(66) Studt, F.; Abild-Pedersen, F.; Bligaard, T.; Sorensen, R. Z.; Christensen, C. H.; Norskov, J. K. *Science* **2008**, *320*, 1320.
(67) Hammer, B. *Top. Catal.* **2006**, *37*, 3.
(68) Inoglu, N.; Kitchin, J. R. *Mol. Simul.* **2010**, *36*, 633.
(69) *CRC Handbook of Chemistry and Physics*; 83rd ed.; CRC Press: Boca Raton, FL, 2002; p 4.132.
(70) Gross, A. *Top. Catal.* **2006**, *37*, 29.
(71) Szanyi, J.; Anderson, S.; Paffett, M. T. *J. Catal.* **1994**, *149*, 438.
(72) Biberian, J.; Van Howe, M. A. *Surf. Sci.* **1984**, *138*, 361.
(73) Passos, F. B.; Schmal, M.; Vannice, M. A. *J. Catal.* **1996**, *160*, 106.
(74) Jin, Y. M.; Datye, A. K.; Rightor, E.; Gulotty, R.; Waterman, W.; Smith, M.; Holbrook, M.; Maj, J.; Blackson, J. *J. Catal.* **2001**, *203*, 292.